



Publication Year	2022
Acceptance in OA @INAF	2024-01-24T16:14:18Z
Title	The Effects of Cosmic Rays on the Chemistry of Dense Cores
Authors	p̃O Donoghue, Ross; VITI, SERENA; PADOVANI, Marco;
DOI	10.3847/1538-4357/ac7963
Handle	http://hdl.handle.net/20.500.12386/34614
Journal	THE ASTROPHYSICAL JOURNAL
Number	934



The Effects of Cosmic Rays on the Chemistry of Dense Cores

Ross O'Donoghue¹ , Serena Viti^{2,1} , Marco Padovani³ , and Tomas James¹ ¹ Department of Physics & Astronomy, University College London, Gower Street, London, WC1E 6BT, UK; ross.o'donoghue.19@ucl.ac.uk² Leiden Observatory, Leiden University, P.O. Box 9513, 2300 RA Leiden, The Netherlands³ INAF-Osservatorio Astrofisico di Arcetri, Largo E. Fermi, 5, I-50125 Firenze, Italy

Received 2022 February 3; revised 2022 June 14; accepted 2022 June 14; published 2022 July 26

Abstract

Cosmic rays are crucial to the chemistry of molecular clouds and their evolution. They provide essential ionizations, dissociations, heating, and energy to the cold, dense cores. As cosmic rays pierce through clouds they are attenuated and lose energy, which leads to a dependency on the column density of a system. The detailed effects these particles have on the central regions still need to be fully understood. Here, we revisit how cosmic rays are treated in the UCLCHEM chemical modeling code by including both ionization rate and H₂ dissociation rate dependencies alongside the production of cosmic ray induced excited species and we study in detail the effects of these treatments on the chemistry of pre-stellar cores. We find that these treatments can have significant effects on chemical abundances, up to several orders of magnitude, depending on the physical conditions. The ionization dependency is the most significant treatment influencing chemical abundances through the increased presence of ionized species, grain desorptions, and enhanced chemical reactions. Comparisons to chemical abundances derived from observations show the new treatments reproduce these observations better than the standard handling. It is clear that more advanced treatments of cosmic rays are essential to chemical models and that including this type of dependency provides more accurate chemical representations.

Unified Astronomy Thesaurus concepts: [Astrochemistry \(75\)](#); [Chemical abundances \(224\)](#); [Cosmic rays \(329\)](#)

1. Introduction

Cosmic rays (CRs) play a vital role in the chemistry of cold (10–30 K), dense ($>10^2 \text{ cm}^{-3}$) molecular clouds as they can pierce deep into them, unlike interstellar UV radiation (for a review see Indriolo & McCall 2013). These high-energy interstellar particles primarily consisting of protons can be heavier elements and electrons, and have large energy ranges, up to zetaelectronvolt energies (Blandford et al. 2014). Although the energies can be high, it is the lower energy CRs ($\leq 1 \text{ TeV}$) that affect the dense interiors (Viti et al. 2013; Padovani et al. 2020). In these regions, CRs have a wide variety of effects, one of the most important is being a producer of atomic hydrogen through the dissociation of H₂ (van der Werf et al. 1988; Montgomery et al. 1995; Li & Goldsmith 2003; Goldsmith & Li 2005; Padovani et al. 2018a). Other important effects are being the dominant source of ionization; regulating the degree of coupling of the gas and the magnetic field; having an important role in the dynamics and the collapse timescale of collapsing clouds (e.g., Padovani et al. 2013, 2014); providing heating and energy to dust grains (de Jong & Kamijo 1973; Shingledecker et al. 2018; Kalvāns & Kalnin 2019; Sipilä et al. 2020, 2021; Silsbee et al. 2021) producing internal UV photons (Prasad & Tarafdar 1983); may have a role on the charge distribution on dust grains (Ivlev et al. 2015); influencing disk growth (Kuffmeier et al. 2020); and affecting deuteration (Caselli et al. 2008). For example, each species ionized by a CR releases an electron. This secondary electron can cause further collisions, which in turn, depending on the energy, can induce more ionization and heating (Ivlev et al. 2021). If a secondary electron does not have enough energy to ionize a species, the species may

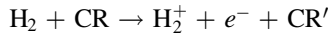
become excited (Shingledecker & Herbst 2018). Excited species produced by CR bombardment have energy levels higher than their base counterparts, allowing these excited species to overcome some reaction barriers that would otherwise be difficult in cold environments. These species have been shown to drive more complex chemistry from reactions that can form interstellar complex organic molecules (Abplanalp et al. 2016).

Although CRs can pierce deep into the molecular clouds, they are still attenuated as they collide and lose energy. The denser the region is, the lower the CR ionization rate becomes (Padovani et al. 2018b). This leads to a dependency of the ionization rate on the density of a region, more precisely on the H₂ column density passed through by CRs.

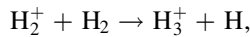
As the Earth is shielded from the low-energy spectrum of CRs through solar modulation (see Potgieter 2013, for a review on solar modulation), measurements of the CR ionization rate taken from Earth are not indicative of measurements in the interstellar medium (ISM), and are in fact lower. Observations of molecules that are dependent or sensitive to the CR ionization rate (for example, H₃⁺ is produced from CR ionization of H₂) can be used as a tracer for the ionization rate (see Viti et al. 2013, for a review). The *typical* value for the CR ionization rate is often taken to be around the order of 10^{-17} s^{-1} (e.g., Spitzer & Tomasko 1968; Solomon & Werner 1971; Herbst & Klemperer 1973; Li & Goldsmith 2003). It is necessary to note that while this may be known as the typical rate, observations show environments with significantly higher rates. Diffuse clouds have been observed with ionization rates in the order of 10^{-16} s^{-1} (Indriolo et al. 2007; Indriolo & McCall 2012) and rates of up to 10^{-14} s^{-1} have been observed within the inner 300 pc of the Galactic Center (Oka et al. 2005; Le Petit et al. 2016). Recently, both Voyager spacecraft passed beyond the heliopause, and have been observing lower energies of the CR spectrum (as low as 3 MeV for both nuclei and electrons)

(Cummings et al. 2016; Stone et al. 2019). This data from the Voyager probes can be used to estimate a lower boundary for the ISM ionization rate (Ivlev et al. 2015; Padovani et al. 2018b). In fact, the local CR flux measured by the Voyager probes is thought to be unmodulated by the solar wind. However, the magnetometers on board the Voyager spacecraft have not yet detected a change in the magnetic field direction, as would be expected if they had passed the heliopause (Gloeckler & Fisk 2015). Furthermore, the ionization rate using the fluxes from Voyager only gives a lower limit to the observational estimates in nearby diffuse molecular clouds (e.g., Indriolo & McCall 2012).

The hydrogen chemistry of CRs is essential to the chemical evolution of a cloud. H_3^+ is fundamental to the production of many polyatomic gas-phase molecules (Herbst & Klemperer 1973) and is formed through the CR ionization reaction:

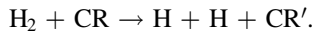


and the subsequent reaction



where H_2 ionization is the rate limiting reaction. In dense clouds, H_3^+ can then react via proton transfer with molecules such as CO (to form HCO^+ or HOC^+), O (forming OH^+), N_2 (forming HN_2^+), and HD (forming H_2D^+). See the review by Indriolo & McCall (2013) for a more in-depth summary.

CRs also dissociate molecular hydrogen in the ISM through the reaction:



In high-density regions, this reaction is the only form of H_2 dissociation, as the UV photons for photodissociation cannot penetrate deep into the cloud. This reaction depends on the CR dissociation rate, which is often taken to be equal to the ionization rate. In chemical networks, however, the rate is often lower than the typical value. In UMIST (McElroy et al. 2013), for example, the H_2 dissociation rate is $1.30 \times 10^{-18} \text{ s}^{-1}$. In Padovani et al. (2018a), it has been shown that the H_2 dissociation rate is higher than is often represented in chemical networks, is not a constant value and is not equal to the ionization rate. The rate is dependent on the secondary electrons produced from CR ionization and can be represented as a function of column density, similar to the CR ionization rate in Equation (1) (Padovani et al. 2018a).

As discussed, it is clear that CRs are extremely important to the chemistry of molecular clouds and their evolution, and hence it is essential that their effects are represented accurately within modern chemical models. This paper aims to improve the handling of CRs in gas-grain chemical models, by introducing both the CR ionization rate and the H_2 dissociation rate as functions of column density and to include the ability to produce excited species and their reactions on the grain. The chemical effects of these additions will be tested on models of collapsing cloud cores. These environments are crucial steps in the early stages of star formation and the effects of CRs on these objects where the gas density increases with time and changes the column density of the core, still need to be investigated. In Section 2, we discuss the chemical modeling and details of the CR treatments we have included for this paper. In Section 3, we describe the effects these treatments have on the chemical abundances of selected species and

discuss the main processes involved in these changes, while in Section 4 we summarize our findings.

2. Modeling

The chemical code selected for this paper is UCLCHEM (Holdship et al. 2017). UCLCHEM is a time-dependent gas-grain chemical code, written in modern Fortran. UCLCHEM is an open-source chemical code, freely available for use and modification. It is diverse in use due to its modular nature. Specific environments (shocks, cores, and collapses) each have their own physics module. UCLCHEM uses separate gas and grain networks. The default gas-phase network used is the UMIST RATE12⁴ network, described in McElroy et al. (2013), and is used for this paper. The grain network used is described in Section 2.1.3 below. For more detailed information on UCLCHEM see Holdship et al. (2017) or visit the UCLCHEM website.

2.1. Treating CRs in UCLCHEM

2.1.1. CR Ionization Rate

In Padovani et al. (2018b), a polynomial fit was developed to express the dependency of the CR ionization rate on column density. We have implemented such a fit into UCLCHEM.

$$\log_{10} \frac{\zeta}{\text{s}^{-1}} = \sum_{k \geq 0} c_k \log_{10}^k \frac{N}{\text{cm}^{-2}}, \quad (1)$$

where k is an integer ranging from 0–9, c_k is the fitting coefficient, and N is the column density.

Equation (1) is used to calculate the ionization rate at each time step and the calculated rate is used in all chemical reactions that involve the CR ionization rate.

Table A1 gives two sets of fitting coefficients. One, labeled as model *L*, describes the trend of the ionization rate as a function of the column density obtained by using the Voyager data; the other, labeled as model *H*, represents the average value of the ionization rate in diffuse clouds (Shaw et al. 2008; Neufeld et al. 2010; Indriolo & McCall 2012; Neufeld & Wolfire 2017).

2.1.2. H_2 Dissociation Rate

Padovani et al. (2018a) evaluated the H_2 dissociation rate based on the same CR interstellar spectra used to compute the ionization rate. In the following, the dissociation rate is parameterized as a function of the column density by using Equation (1) with the coefficients listed in Table A1. Similar to the CR ionization treatment, the dissociation rate can now be calculated at each time step of the model. However, this handling of the dissociation rate can only be activated if the CR ionization dependency is also activated and is automatically set to the same model (*L* or *H*) as the CR ionization dependency.

Figure 1 shows how the CR ionization rate and H_2 dissociation rate differ from the *standard* handling of UCLCHEM (i.e., the fixed, user-defined value) under increasing density. This particular example shows all three models at a $\times 1$ ionization factor. UCLCHEM handles the ionization rate in multiples of $1.3 \times 10^{-17} \text{ s}^{-1}$, so an ionization factor of $\times 1$ will correspond to an ionization rate of $1.3 \times 10^{-17} \text{ s}^{-1}$ and a H_2

⁴ www.udfa.net

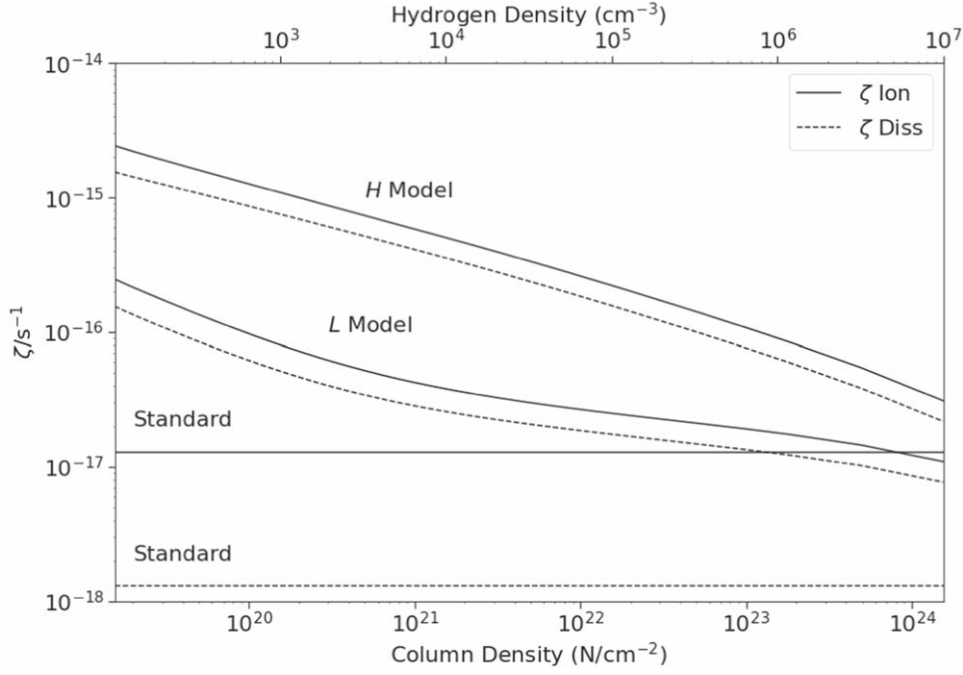


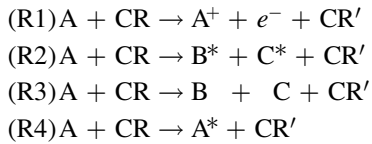
Figure 1. Figure showing the CR ionization rate dependency (solid line) and the H_2 dissociation rate dependency (broken line) compared to the standard UCLCHEM handling. For these models, we use a cloud size of 0.05 pc.

dissociation rate of $1.3 \times 10^{-18} \text{ s}^{-1}$ for the standard handling. UCLCHEM calculates the column density by multiplying the size of the cloud (in parsecs) by the total hydrogen density (per cubic centimeter).

2.1.3. Excited Species

UCLCHEM uses a user-defined grain network, separate from the gas-phase network. The default grain network that is provided with UCLCHEM handles some basic CR and photon interactions, freeze-out reactions, and chemical desorption and diffusion reactions. This network was used for this paper, with the additions of excited species production and reactions due to CRs: these excited species are added using the principles described in detail in Shingledecker & Herbst (2018) and used in Shingledecker et al. (2018).

The underlying principles are that CR bombardments of a solid species generally have one of the following outcomes:



where A is the target species, B and C are dissociated products and * represents an excited species. The reaction rates for these interactions are defined in Shingledecker & Herbst (2018) and follow the formula:

$$k_{Rn} = G_{Rn} \left(\frac{S_e}{100 \text{ eV}} \right) \left(\phi_{\text{ST}} \left[\frac{\zeta}{10^{-17} \text{ s}^{-1}} \right] \right), \quad (2)$$

where G_{Rn} is the radiochemical yield for the reaction pathway Rn, (Rn being R1–R4 above), and S_e is the electronic stopping cross section. ϕ_{ST} is the integrated Spitzer–Tomasko CR flux (from 0.3 MeV–100 GeV) and has a value of $8.6 \text{ cm}^{-2} \text{ s}^{-1}$. ζ is a CR ionization rate scaling factor for the CR flux.

Once produced, an excited species will either react with another solid species, or relax back to the ground energy state. The excited species reaction proceeds at the rate:

$$k_{st} = f_{br} \left[\frac{v_0^B + v_0^A}{N_{\text{site}} n_{\text{dust}}} \right], \quad (3)$$

where f_{br} is the branching ratio, v_0 is the vibrational frequency of the species, N_{site} is the number of physisorption sites on the grain, and n_{dust} is the dust density.

2.2. Modeling Pre-stellar Cores

The effects of these additions will be studied in the cases of pre-stellar cores. Pre-stellar cores represent the early stages of low-mass star formation and have densities in the range of $\sim 10^4$ – 10^7 cm^{-3} , depending among other things, on their evolutionary stage. The models will be set to mimic these regions; in each case, the model will start at an initial density of 10^2 cm^{-3} . At $\sim 10^6$ yr, the models will collapse in freefall to a specific final density. To cover the density range, the models have four possible final densities: 10^4 , 10^5 , 10^6 , or 10^7 cm^{-3} . After collapsing, the models are set to run with static conditions until a final time of 10^8 yr is reached, in order to investigate the chemical evolution over time. To determine the influence that temperature and radiation field may have on the CR ionization dependency, each will be varied independently (see Table 1 for values). Note: UCLCHEM assumes 1 Habing to be the Galactic radiation field strength. The chemical species that will be analyzed are H_2O , CS, $\text{NH}_{3(\text{grain})}$, N_2H^+ , NH_3 , $\text{CO}_{(\text{grain})}$, HCO^+ , $\text{H}_2\text{O}_{(\text{grain})}$, and $\text{CO}_{2(\text{grain})}$. These species are important as some act as tracers of the gas phase of pre-stellar cores, their regions, and physical conditions (CS, N_2H) (Lee et al. 1999), and some are key species for grain chemistry and the chemical complexity (NH_3 , $\text{NH}_{3(\text{grain})}$) (Rodgers & Charnley 2001) and others are some of the most abundant species found in these regions ($\text{H}_2\text{O}_{(\text{grain})}$, $\text{CO}_{(\text{grain})}$, and $\text{CO}_{2(\text{grain})}$) (Öberg et al. 2011).

Table 1
Parameters of the Model Grid for Ionization and H₂ Dissociation

Parameter	Value	Description
Final density (cm ⁻³)	10 ⁴ /10 ⁵ /10 ⁶ /10 ⁷	Selects the final density of the model
Initial temperature (K)	10/20/30	Selects the gas temperature
Radiation field (Habing)	1/10/100	Adjusts the local interstellar radiation field
ζ	$\times 1/\times 10/\times 100$	Adjusts the CR ionization rate as a multiplicative of $1.3 \times 10^{-17} \text{ s}^{-1}$ for the standard UCLCHEM handling or adjust the ionization dependency if desired
Modified ionization	Basic/ <i>L</i> model/ <i>H</i> model	Selects the <i>basic</i> UCLCHEM handling (fixed, user-defined value) or the updated ionization rate dependency
Modified dissociation	Off/On	Toggles modified H ₂ dissociation rate (only active with <i>L</i> or <i>H</i> ionization models)
Excited species	Off/On	Toggles inclusion of excited species

The CR ionization dependency, H₂ dissociation dependency, and excited species production and reactions will all be tested individually as well as combined. To test the effects of the CR ionization dependency, under each condition, models will be run with the CR ionization dependence turned off and compared to the same conditions with the *L* and the *H* model dependencies activated. The H₂ dissociation rate dependency can only be activated when the *L* or *H* ionization model is also selected. To test the influence of the H₂ dissociation rate, *L* and *H* models with the dissociation dependency disabled will be compared to the same model with the dissociation dependency activated. The excited species can be activated without the CR or H₂ dissociation rate dependencies. As such their effects will be examined independently of the other additions and then combined together. Table 1 shows a summary of the parameters investigated, their values, and their descriptions. In total, a grid of 280 models were run.

3. Results

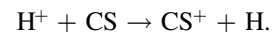
When discussing the influence of the CR ionization rate dependency on the chemistry of pre-stellar cores, our simulated core evolution is split into three phases. The pre-collapse phase covers the period of up to $\sim 10^6$ yr and represents the period of time leading up to the beginning of the cloud collapse (abundances are examined at a time of 10^5 yr). This phase of the model has a gas density of 10^2 cm^{-3} , until the collapse phase where density begins to increase. The cloud collapse phase represents the time at which the cloud is undergoing collapse in freefall and occurs between $\sim 10^6$ and 6×10^6 yr, depending on the final density. The density here is increasing over this period from the initial density to the selected final density of the model. The post-collapse phase represents the period of static density, after the cloud collapses to the designated final density. The post-collapse phase will always have a constant density equal to the selected final density parameter of the individual model. In order to assess trends in our simulations, we set a lower limit for *observable* fractional abundances of 10^{-13} ; below this fractional abundance, changes across the parameter space will be considered irrelevant. Additionally, any changes in abundances that are below a

factor of 3 will not be discussed, as these differences are not likely observable. Any abundance changes that do not obey the following trends are listed in Table 2.

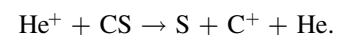
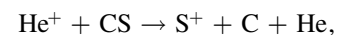
3.1. Density Dependent Ionization Rates

Figure 2 shows the effects of adding the ionization rate density dependency on chemical abundances for a final density of 10^4 cm^{-3} , a temperature of 10 K, a radiation field strength of 1 Habing, and an un-adjusted ionization rate factor of $\times 1$. Table A2 summarizes the abundance trends. In the pre-collapse phase, the addition of the ionization rate dependency results in reduced abundances for all our selected species. The same trend is seen for both the *L* and *H* models with the *H* model having enhanced effects (i.e., larger reductions in abundances, up to 3 orders of magnitude, see Table A2). We note that during this phase of the pre-stellar core evolution, the CR ionization rate is indeed higher by almost a factor of ~ 20 for the *H* model compared to the value used for the standard model, which proves to be very destructive in the early stages.

This destruction comes from both the increased presence of ionized species and increased grain desorptions. H⁺ and He⁺ are two ions that play important roles in gaseous destruction. For example, with CS, the main destruction route during the pre-collapse phase under the standard model comes from its photodissociation into S and C with some contribution from photoionization and reactions with ionized species. The increased ionization rates for the *L* and the *H* models result in increased abundances for the H⁺ and He⁺ ions. The H⁺ ion plays a part in the CS destruction through the route



The importance of this reaction is enhanced with the *L* model and is significantly more dominant for the *H* model. The *H* model also has higher destruction contributions from the He⁺ ion via the routes



A second example of this is H₂O, where the destruction in the standard model has some contributions from C⁺ and H₂O

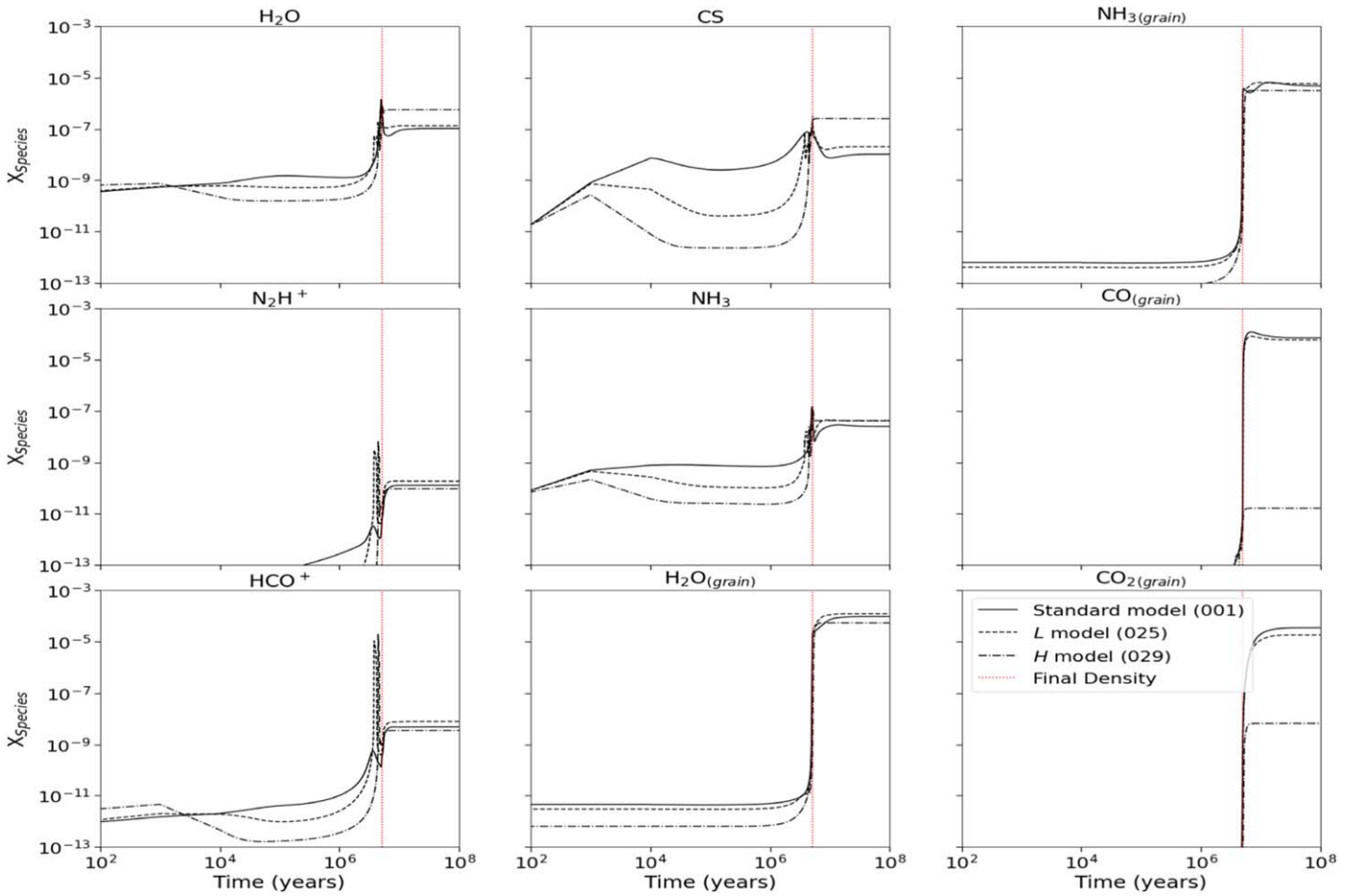


Figure 2. Plot showing the effect of the *L* and *H* ionization models (short- and long-dashed black lines, respectively) on chemical abundances over time compared to the basic UCLCHEM handling (solid black line). These models have a final density of 10^4 cm^{-3} , an initial temperature of 10 K, a radiation field of $\times 1$, and an ionization rate of $\times 1$. The red line represents the time at which the final density is reached and the numbers in the legend represent the model number identifier.

Table 2
The Post-collapse Species, Conditions, and the Behavior That Do Not Follow the General Trends of the Ionization Dependency

Species	Conditions	Behavior
Ionization rate dependency		
H ₂ O	10^6 cm^{-3} , <i>H</i> model	Increase in abundance larger than other densities.
N ₂ H ⁺	10^5 cm^{-3} , <i>H</i> model	Only density to undergo a notable change (increased abundance).
NH ₃	10^6 cm^{-3} , <i>H</i> model	Only density to undergo a notable change (increased abundance).
HCO ⁺	10^6 cm^{-3} , <i>H</i> model	Increase in abundance larger than other densities.
Ionization rate dependency with parameter variations		
N ₂ H ⁺	20 K, 10^6 cm^{-3} , <i>H</i> model 30 K, 10^6 cm^{-3} , <i>H</i> model	Change in abundance greater than other densities. Only condition to undergo a change in abundance at 30 K. Abundance not as reduced as at 20 K.
NH ₃ (grain)	30 K, 10^5 cm^{-3} , <i>H</i> model	Only condition to undergo a change in abundance at 30 K. Abundance further reduced than at 20 K.
CO ₂ (grain)	30 K, 10^5 cm^{-3} , <i>H</i> model	Only condition to undergo a change in abundance at 30 K. Abundance further reduced than at 20 K.
CS	100 times radiation field, 10^4 cm^{-3} , <i>H</i> model	Abundance is not as reduced as at 10 times radiation field.
H ₂ O(grain)	100 times initial ionization rate, 10^5 cm^{-3} , <i>H</i> model	Reduction in abundance is greater than at 10^4 cm^{-3} .

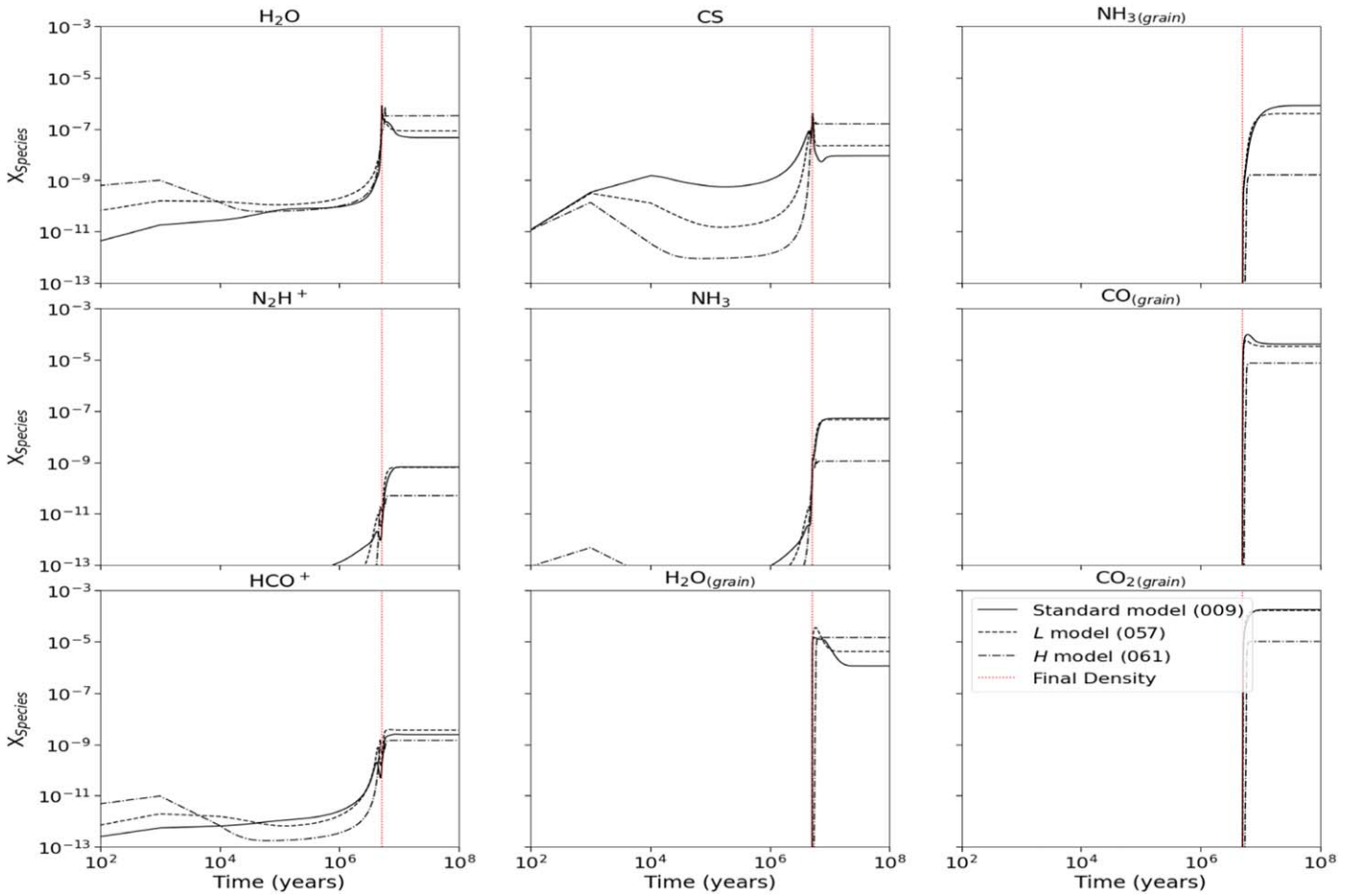
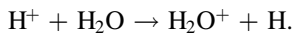


Figure 3. Plot showing the effect of the *L* and *H* ionization models (short- and long-dashed black lines, respectively) on chemical abundances over time compared to the basic UCLCHEM handling (solid black line). These models have a final density of 10^4 cm^{-3} , an initial temperature of 20 K, a radiation field of $\times 1$, and a zeta of $\times 1$. The red line represents the time at which the final density is reached and the numbers in the legend represent the model number identifier.

reactions but is mostly dominated by H_2O photodissociation into OH and H. Similarly to CS, the increased abundances of H^+ at higher ionization rates drove the destruction of H_2O through the reaction



While gaseous species undergo reduced abundances due to ions, solid species undergo these reductions via CR-induced desorptions. For example, $\text{H}_2\text{O}_{(\text{grain})}$ in the standard model is primarily destroyed by CR-induced UV desorptions. With the increased ionization rates of the *L* model, direct CR desorption also begins to take place. The even higher ionization rates of the *H* model result in both the CR-induced UV desorption and the direct CR desorptions becoming more efficient, resulting in the reduced abundances seen.

During the post-collapse phase, species only undergo notable changes in abundance with the *H* model. Gas-phase H_2O and CS have increased abundances while the solid phase $\text{CO}_{(\text{grain})}$ and $\text{CO}_2_{(\text{grain})}$ show decreased abundances. In this case, the solid phase species tend to undergo more destruction, with $\text{CO}_{(\text{grain})}$ and $\text{CO}_2_{(\text{grain})}$ decreasing in abundance by over 3 orders of magnitude and the gaseous species undergo increases up to a factor of 20. While these large decreases in abundances are mainly caused by CR-induced desorptions, there are also contributions from reduced formation rates. CO freeze-out to $\text{CO}_{(\text{grain})}$ is the dominant formation route during the cloud collapse. Under the *H* model, this formation method is

significantly inhibited during the collapse phase, reducing the amount of freeze-out taking place. $\text{CO}_2_{(\text{grain})}$ is also affected by the CO freeze-out inhibition. The primary formation route for $\text{CO}_2_{(\text{grain})}$ comes from the diffusion of $\text{CO}_{(\text{grain})}$ and $\text{OH}_{(\text{grain})}$. Reduced abundances for both of these species with the *H* model inhibit the amount of $\text{CO}_2_{(\text{grain})}$ formation. The combination of less formation and more desorption results in these significant decreases seen with the *H* model. These increased desorptions can also influence the gas-phase species. After the collapse, the primary H^+ destruction route for H_2O is no longer efficient; this fact coupled with the increased desorptions of $\text{H}_2\text{O}_{(\text{grain})}$, result in the increased post-collapse abundances seen. Other species, like CS, are not as reliant on desorptions. After the collapse, the primary formation route for CS comes from the photodissociation of H_2CS into CS and H_2 . The H_2CS molecule also shows increased abundances for the *L* model and significantly so for the *H* model, which in turn leads to more efficient photodissociation.

When the final density is increased, this reduces the effects of the addition of ionization dependency. $\text{CO}_{(\text{grain})}$ and $\text{CO}_2_{(\text{grain})}$ are prime examples of this effect, as the large decreases in abundances seen at 10^4 cm^{-3} are no longer present at higher densities (changes in abundance are now under an order of magnitude). The reduced ionization rates as density increases are the main cause of this feature through reduced CR desorptions. Also, under these conditions, CO freeze-out

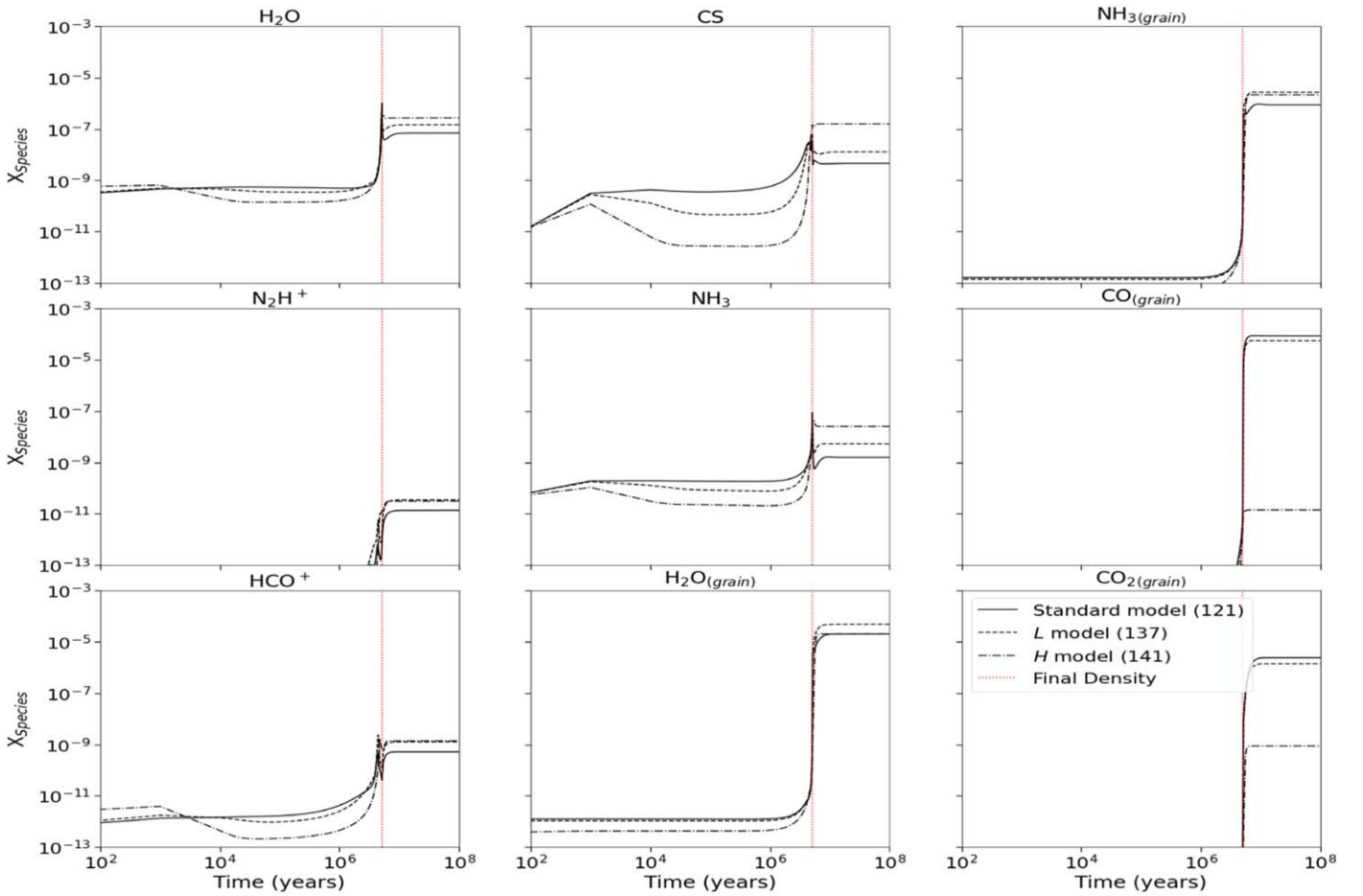


Figure 4. Plot showing the effect of the *L* and *H* ionization models (short- and long-dashed black lines, respectively) on chemical abundances over time compared to the basic UCLCHEM handling (solid black line). These models have a final density of 10^4 cm^{-3} , an initial temperature of 10K, a radiation field of $\times 10$, and a zeta of $\times 1$. The red line represents the time at which the final density is reached and the numbers in the legend represent the model number identifier.

during the collapse is not inhibited by the increased ionization rates. This, along with the lower desorptions, leads to the reduced effects of the ionization dependency.

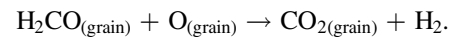
3.1.1. Effects Due to Temperature Variations

Figure 3 shows the *L* and *H* models with an increased initial temperature of 20 K, while Table A3 summarizes the effects on the *L* and *H* models with initial temperatures of 20 K and 30 K. During the pre-collapse phase, when the temperature is increased, only CS and HCO^+ show notable changes. Both still show a reduction in abundance with the ionization dependency, but the reduction is lower at higher temperatures (CS is reduced by over 2 orders of magnitude and HCO^+ is reduced by up to a factor 6 for the *H* model). At higher temperatures, only H_2O , CS, and HCO^+ have abundances above the set limit of 10^{-13} . For the post-collapse phase, increasing the temperature to 20 K results in larger changes in abundance than in the *H* model for solid and gas-phase NH_3 . However, CS, $\text{CO}_{(\text{grain})}$, and $\text{CO}_{2(\text{grain})}$ instead undergo less of a change than at 10 K (significant in the cases of $\text{CO}_{(\text{grain})}$ and $\text{CO}_{2(\text{grain})}$, where the large reduction in abundance at 10 K for the *H* model is no longer seen). At 30 K, only CS and NH_3 have their abundance change by over a factor of 3 (both by a factor of ~ 8) and in both cases, these changes are less than they are at 20 K for the *L* model. Increasing the density at these

temperatures has a similar effect as that at 10 K (i.e., reduced changes as density increases).

Gas-phase NH_3 abundances are strongly influenced by the solid phase NH_3 abundances. Gas-phase formation comes completely from grain desorptions. $\text{NH}_{3(\text{grain})}$, however, at 10 K under all models, is formed via $\text{H}_{(\text{grain})}$ and $\text{NH}_{2(\text{grain})}$ diffusion. As the temperature increases, this reaction becomes less dominant, particularly during the pre-collapse phase and with the *H* model at 30 K. In this case, there is no formation from the diffusion reaction, which results in $\text{NH}_{3(\text{grain})}$ having abundances below the set limit.

$\text{CO}_{2(\text{grain})}$, at higher temperatures, relies less on $\text{CO}_{(\text{grain})}$ diffusion. During the post-collapse phase, the primary formation rate comes from the diffusion reaction:



The reduced changes in abundance for $\text{CO}_{2(\text{grain})}$ here are a result of the $\text{H}_2\text{CO}_{(\text{grain})}$ abundances. Under the *L* model, $\text{H}_2\text{CO}_{(\text{grain})}$ has higher abundances, resulting in more diffusion, which is balanced out by the increased desorption of $\text{CO}_{2(\text{grain})}$, leading to little change from the standard model. The *H* model on the other hand, still sees a reduction in abundance, which is a result of the increased desorptions, but the reduction is not as severe as it is at 10 K, due to the *H* model having increased $\text{O}_{(\text{grain})}$ abundances for more diffusion.

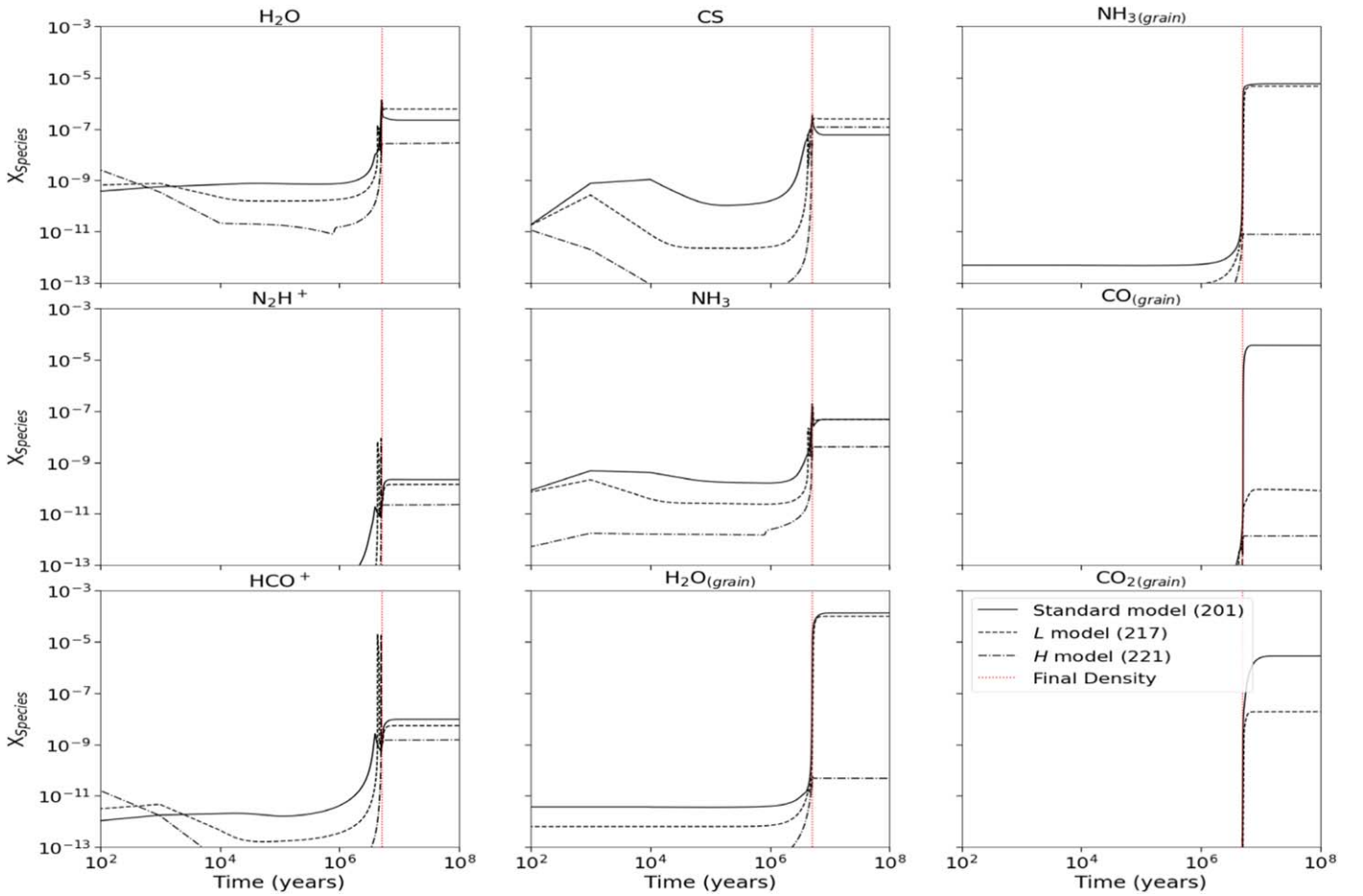


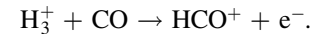
Figure 5. Plot showing the effect of the *L* and *H* ionization models (short- and long-dashed black lines, respectively) on chemical abundances over time compared to the basic UCLCHEM handling (solid black line). These models have a final density of 10^4 cm^{-3} , an initial temperature of 10K, a radiation field of $\times 1$, and a zeta of $\times 10$. The red line represents the time at which the final density is reached and the numbers in the legend represent the model number identifier.

3.1.2. Effects Due to Variations in the Radiation Field Strength

Figure 4 shows the differences between the standard model and the models where the new treatment of the cosmic ionization rate is included, when the radiation field is increased by a factor of 10. Table A3 summarizes the results of enhancing the radiation field by factors of 10 and 100.

In the pre-collapse phase, enhancing the radiation factor by a factor of 10 reduces the changes in abundance produced by the ionization dependency, which are further reduced when the radiation field is increased by a factor of 100 (changes in abundance are up to 1 order of magnitude, see Table A3). During the post-collapse phase, in general, increasing the radiation field enhances the effects of the ionization rate dependency. At a radiation field of 100 Habing, only H_2O , CS, NH_3 , and HCO^+ are above the 10^{-13} threshold and have increased abundances compared to the standard model. Changes in H_2O , NH_3 , and HCO^+ are enhanced by ~ 1 , ~ 2 , and ~ 1 orders of magnitude, respectively. The large increase in abundance for NH_3 comes from desorption from the grains. Under the standard model and the *L* model, $\text{NH}_{3(\text{grain})}$ abundances are below the set limit. This is not the case for the *H* model. The increased grain abundance here is due to the diffusion of $\text{H}_{(\text{grain})}$ and $\text{NH}_{2(\text{grain})}$. Under these conditions, both of these species have significantly higher abundances with the *H* model than the *L* or standard model. This increases $\text{NH}_{3(\text{grain})}$ formation, which then can desorb into the gas phase. For

HCO^+ , under the increased radiation field, there are two main formation routes, photoionization of HCO and the H_3^+ reaction:



Under the *L* and *H* models, both CO and H_3^+ have much higher abundances, leading to the increased production of HCO^+ . When the density is increased above 10^4 cm^{-3} , there are no significant differences between the effects of the ionization dependency at the standard radiation field strength and the effects at increased strengths.

3.1.3. Effects Due to the Variations in the Initial CR Ionization Rate

Figure 5 shows the effects of increasing the ionization rate by a factor of 10 on the chemical abundances with the ionization rate dependency. Table A3 summarizes the results of increasing the rate by factors of 10 and 100.

Increasing the initial ionization rate in this manner proves to be very destructive both with and without the ionization dependency, particularly in the pre-collapse phase. Many species have abundances below the set limit with this increased ionization rate factor. Those that are visible show much larger abundance reductions (up to 2 orders of magnitude, see Table A3) than at an un-adjusted rate. During the post-collapse phase, increasing the ionization rate by factors of 10 and 100, increases the influence of the ionization dependency. Species that had no notable changes under the standard rate now show

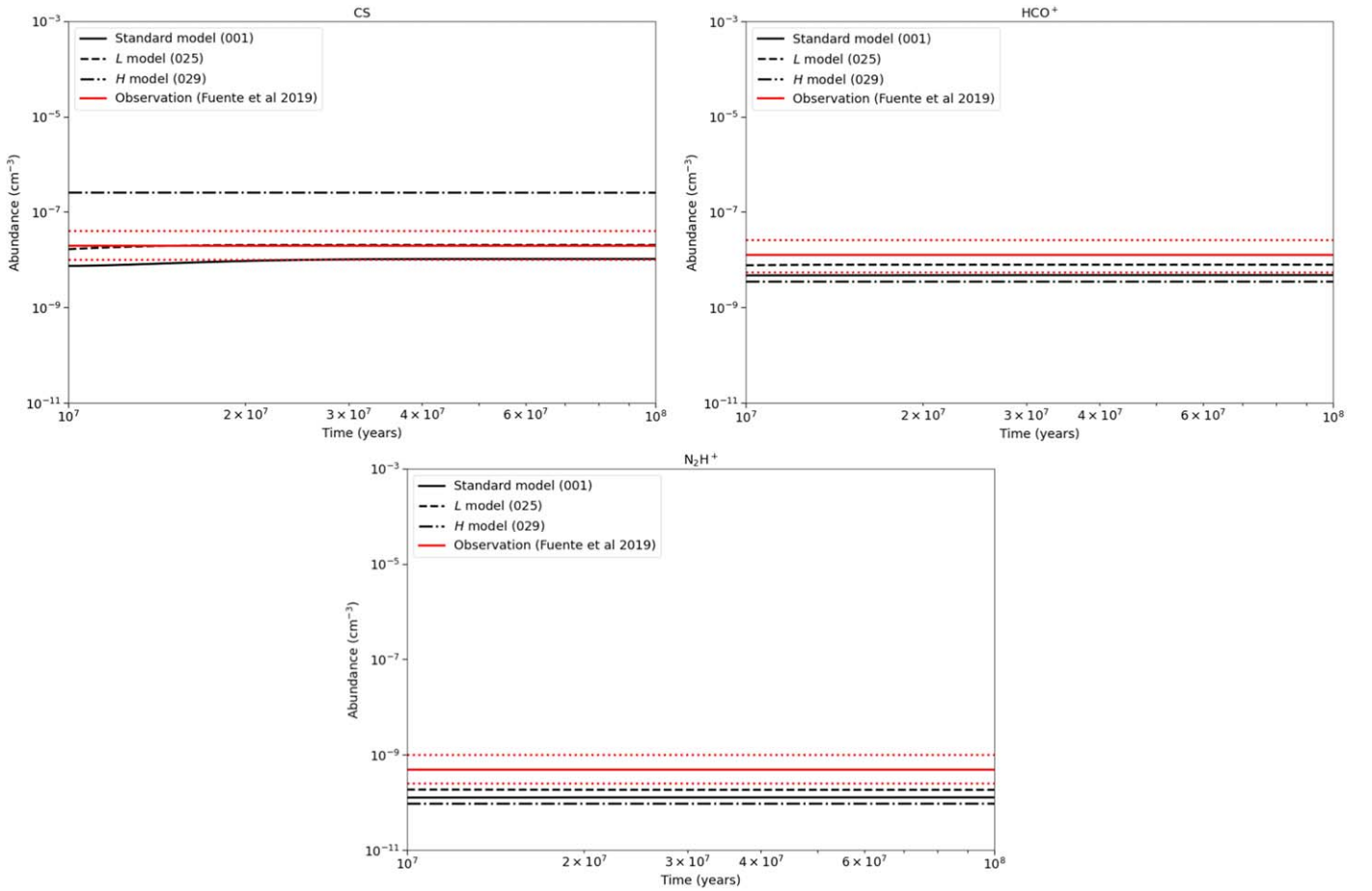


Figure 6. Figure showing the upper and lower limits of species in TMC-1, derived from Fuente et al. (2019). The figures compare observed abundances of CS (top left), HCO^+ (top right), and N_2H^+ (bottom) limits to UCLCHEM post-collapse models. The red dotted lines show the upper and lower limits.

reduced abundances. $\text{CO}_{(\text{grain})}$ and $\text{CO}_{2(\text{grain})}$ again are particularly affected, showing reductions of up to 7 orders of magnitude. These effects are more enhanced in the $\times 100$ initial ionization rate. As with the other conditions, cores of higher densities show reduced effects from the ionization dependency, even with the enhanced initial CR ionization rate. These trends originate for the same reasons as for the models with a standard initial CR ionization rate but are more pronounced (e.g., increased ions and desorption).

3.2. Density Dependent Dissociation Rates

Table A4 summarizes the only cases where the H_2 dissociation rate has any effect. In short, under an enhanced radiation field of 100 times the galactic one, an increase in abundance was seen for the solid species (by a factor of ~ 4), at a low density (10^4 cm^{-3}) and only for the *L* model. The other notable effect is seen at an increased initial ionization rate of $\times 10$, for $\text{CO}_{(\text{grain})}$, and also at 10^4 cm^{-3} with the *L* model, where a significant increase in abundance (~ 3 orders of magnitude) is seen. This large increase in abundance can be traced to the diffusion of $\text{H}_{(\text{grain})}$ and $\text{CO}_{(\text{grain})}$ into $\text{HCO}_{(\text{grain})}$. Under these conditions, this is the dominant destruction route for $\text{CO}_{(\text{grain})}$. Under the H_2 dissociation rate, this reaction pathway is severely inhibited, reducing the destruction of $\text{CO}_{(\text{grain})}$ during and after the collapse. Abundances of $\text{H}_{(\text{grain})}$ here are also lower for the H_2 dissociation dependency model, which may explain the inhibition.

3.3. Excited Species

Table A4 summarizes the only conditions where the inclusion of the excited species had a notable effect on the abundances of the selected species. At an increased temperature of 30 K, N_2H^+ shows a reduced abundance by a factor of 4 at a density of 10^5 cm^{-3} . Increasing the initial ionization rate by a factor of 10 reduces $\text{CO}_{2(\text{grain})}$ abundances at a density of 10^4 cm^{-3} . The most significant effects come from increasing the ionization by a factor of 100. While the higher ionization rates provide more excitations, the increased destruction of the species is not only from their excitation and subsequent reactions. $\text{CO}_{(\text{grain})}$, for example, is also heavily affected by the $\text{H}_{(\text{grain})}$ and $\text{CO}_{(\text{grain})}$ diffusion reaction. The addition of the excited species also produces higher abundances of $\text{H}_{(\text{grain})}$, which increased the amount of $\text{CO}_{(\text{grain})}$ diffusion.

3.4. Density Dependency with Excited Species

In this section, models with both the ionization rate and dissociation rate dependencies activated are compared with and without the inclusion of excited species. Table A5 shows the effects under standard conditions (10 K initial temperature, radiation field strength of 1 Habing, and an initial ionization factor of $\times 1$). $\text{CO}_{(\text{grain})}$ and $\text{CO}_{2(\text{grain})}$ are the main species affected, and have reduced abundances when the excited species are included. These reduced abundances are caused via the same destruction methods discussed in the previous subsection.

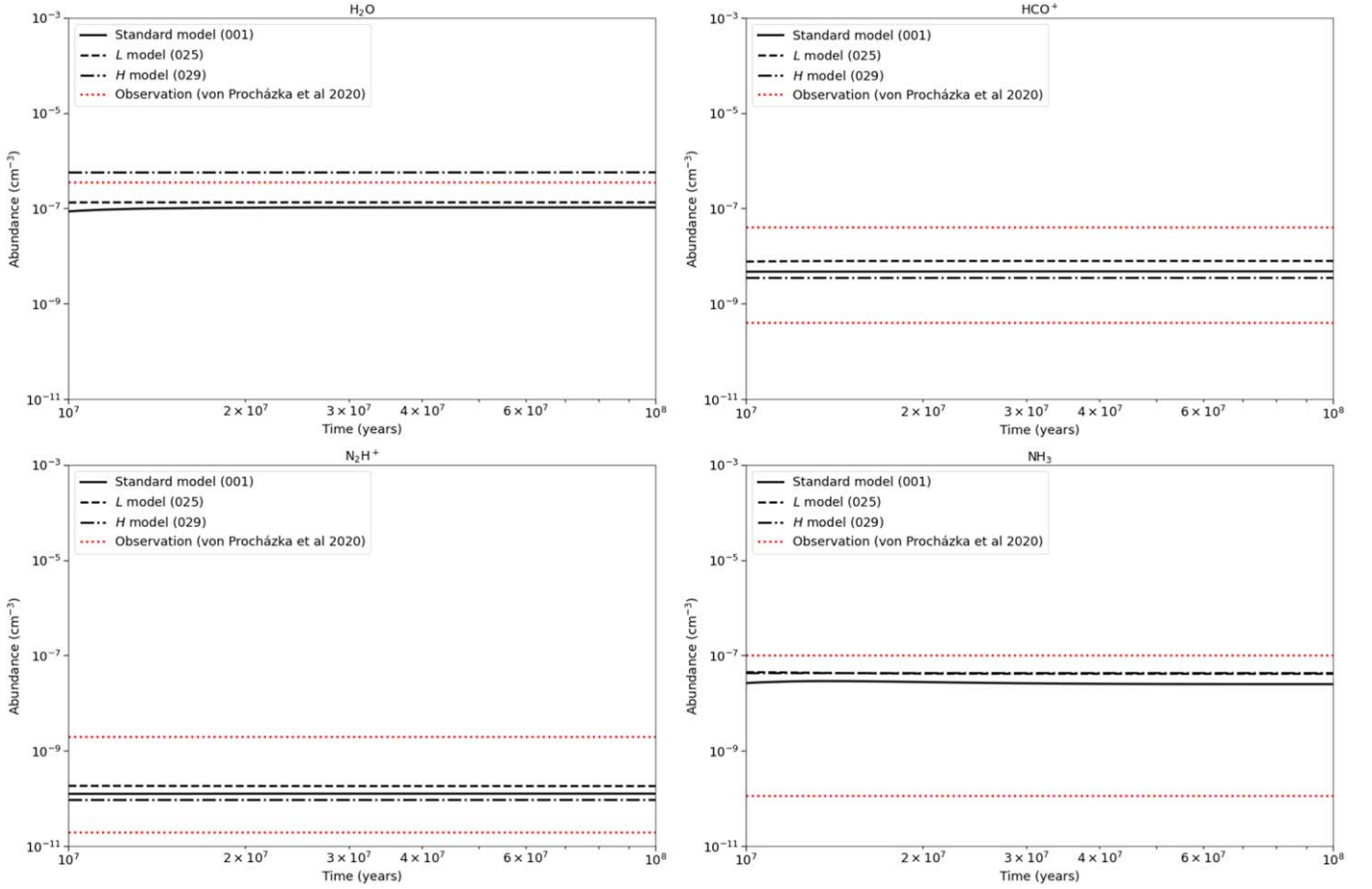


Figure 7. Figure showing the upper and lower limits of species in TMC-1, derived from von Procházka & Millar (2020). The figures compare observed abundances of H_2O (top left), HCO^+ (top right), N_2H^+ (bottom left), and NH_3 (bottom right) limits to UCLCHEM post-collapse models. The red dotted lines show the upper and lower limits (for H_2O there are only upper limits).

3.4.1. Effects Due to Varying the Parameters

When the excited species are included with the CR ionization and H_2 dissociation in the chemical models, the effects of varying the temperature and radiation field strength are reduced, while the effects of varying the ionization factor are increased. As such these effects are quickly summarized here.

Increasing the initial temperature and increasing the radiation field strength both inhibit the effects of including the excited species. Under a higher temperature, including the excited species only has an effect on N_2H^+ (this is at 30 K and a density of 10^7 cm^{-3} with the H model only) where the species show an increased abundance. Increasing the radiation field strength only has an inhibitory effect on lower densities. At 10^5 cm^{-3} and above, there are no differences between 1, 10, and 100 Habing.

Including the excited species with increased initial ionization rates of 10 and 100 times the standard handling has a greater effect than at the $\times 1$ value. The changes in abundance are both larger and seen for more species. At 10 times the standard initial ionization rate, effects are only seen with the H model at 10^5 and 10^6 cm^{-3} . Under these conditions, most species undergo reduced abundances (several orders of magnitude for CS , $\text{CO}_{(\text{grain})}$, HCO^+ and $\text{CO}_{2(\text{grain})}$). Under an increased rate of 100 times the standard handling, the species undergo larger reductions, under the same densities but with the L model

instead. Similar reductions are also seen here at 10^7 cm^{-3} in both the L and H models.

3.5. Comparison to Observations

In this section, we qualitatively compare our models to a set of observations from the cyanopolyne peak (CP or Core D; Hirahara et al. 1992) of the molecular cloud TMC-1, which is thought to currently undergoing rapid core formation (Choi et al. 2017). This core was chosen as it has been well studied and its density is expected to be around 10^4 cm^{-3} with a temperature of about 10 K. The density of 10^4 cm^{-3} is a good candidate for this study, as the effects of the ionization rate dependency are greater due to the low density.

Both von Procházka & Millar (2020) and Fuente et al. (2019) report chemical abundances of the CP region. Fuente et al. (2019) report molecular abundances derived from observations using the IRAM 30 m (3 mm and 2 mm) and the Yebes 40 m telescopes. Depending on the setup, the IRAM 30 m has a spatial resolution of $\sim 29''$ and the Yebes 40 m has an HPBW of $42''$ or $84''$. On the other hand, von Procházka & Millar (2020) report a collection of upper and lower abundance limits obtained from ~ 20 other studies (see Table 2 in von Procházka & Millar 2020), with the emphasis that focusing on upper and lower limits somewhat mitigates the errors in observations and modeling.

Figure 6 shows the data reported in Fuente et al. (2019), compared to the UCLCHEM models at 10 K and a final density of 10^4 cm^{-3} with and without the inclusion of the CR ionization rate dependency during the post-collapse phase. The standard UCLCHEM model for CS and HCO^+ tends to display abundances that are near the lower limit, while the L model is closer to the central values. The H model overpredicts the abundance for CS and underpredicts the abundance for HCO^+ . With N_2H^+ , all models underpredict the abundance, with the L model being the closest and the H model underpredicting the most.

Figure 7 shows data reported in von Procházka & Millar (2020), also compared to the UCLCHEM models at 10 K and a final density of 10^4 cm^{-3} with and without the inclusion of the CR ionization rate dependency during the post-collapse phase. In the cases of HCO^+ , N_2H^+ , and NH_3 , for all models the post-collapse abundances are within the upper and lower limits of the observations. In von Procházka & Millar (2020) only an upper limit is noted for H_2O . In this case, the H model exceeds the stated limit while the L and basic models do not.

In the case of this region in TMC-1 and the compared species, the L model of the ionization dependency appears to perform the best out of the three models. The H model overpredicts or underpredicts the abundances on several occasions, suggesting this upper limit for the ionization rate may in fact be too high.

One caveat that must be addressed is how UCLCHEM handles grains. This version of UCLCHEM considers a grain to be a single layer (i.e., no distinction between grain surface and bulk). It is therefore necessary to speculate on the effects a multilayer grain approach may have on these results. Species in the bulk are somewhat shielded from CR impacts and the subsequent desorptions. As CR desorptions are critical to the changes in the abundance seen for species like $\text{CO}_{2(\text{grain})}$ and $\text{CO}_{(\text{grain})}$, it is likely the changes in abundance seen with the inclusion of the CR ionization dependency will be less significant. Excited species in the bulk are also more protected. Desorptions from excitations and excited reactions would be reduced with a greater emphasis on relaxations, again reducing the effects we see in our models.

4. Summary

In this paper, we improve the treatment of CRs in the gas-grain time-dependent chemical code UCLCHEM by including the dependency of the CR ionization and H_2 dissociation rates on the column density of the gas, as well as the excited species due to the CRs on the grains. We then evaluate the effects of these additions on the chemistry of pre-stellar cores. It is evident that the CR ionization rate dependency on the column density of the core is the most influential of the treatments, with the inclusion of excited species on the grains playing roles only under specific conditions. Our conclusions can be summarized as follows:

1. In the low densities of the pre-collapse phase ($\sim 10^2 \text{ cm}^{-3}$) the ionization rate dependency is very destructive due to CR-induced desorptions and the production of chemically important ions.
2. After the core collapses, the inclusion of the dependency of the CR ionization rate on the column density of the core leads to increased grain desorptions, which decrease solid species abundances (and subsequently increases the

- abundances of gaseous species), and species like H_2O , $\text{CO}_{(\text{grain})}$ and $\text{CO}_{2(\text{grain})}$ are particularly affected by this. Other gaseous species, like CS show increased abundances from dissociations of larger molecules like H_2CS .
3. Changing the physical parameters of the cloud alters the impact of the new treatments in a nontrivial manner. Higher densities have lower ionization rates with the dependency, reducing the changes in abundance seen for all species. Increasing the temperature also has a similar effect on CS, $\text{CO}_{(\text{grain})}$, and $\text{CO}_{2(\text{grain})}$ (increased formation rates balance out the destruction from the CRs), while NH_3 shows lower abundances due to less $\text{NH}_{3(\text{grain})}$ formation and subsequent desorption. Increasing the radiation field strength enhances the effects of the ionization dependency, which occurs as a result of grain and gas formation routes. NH_3 , for example, undergoes increased abundances with the H model due to higher $\text{NH}_{3(\text{grain})}$ grain formation and desorption, while HCO^+ undergoes larger changes due to formation in the gas via H_3^+ and CO.
4. The H_2 dissociation rate dependency and the inclusion of excited species only affect the chemistry of some of the investigated species under specific conditions. The H_2 dissociation dependency increases the abundances of some solid species for the L model under two conditions, a $\times 10$ ionization rate and a $\times 100$ radiation field strength. $\text{CO}_{(\text{grain})}$ results in these increases in abundances due to the inhibition of its primary destruction route, from a reduced abundance of the $\text{H}_{(\text{grain})}$ reactant. The excited species reduce solid abundances at higher ionization rates, particularly with $\text{CO}_{2(\text{grain})}$ and $\text{CO}_{(\text{grain})}$. While the excitations and subsequent reactions reduced the solid abundances, destruction also comes from reactions with $\text{H}_{(\text{grain})}$ (which also sees higher abundances under these conditions).
5. Chemical models with and without the ionization dependency were compared to molecular abundances in the TMC-1 cyanopolyne peak from Fuente et al. (2019) and von Procházka & Millar (2020). The comparisons show that the L model of the dependency tends to reproduce abundances more reliably than the standard handling or the H model. All models had more difficulty reproducing N_2H^+ abundances (the L model still performed better). The H model predicted abundances outside the Fuente et al. (2019) observational limits for both CS and HCO^+ and overpredicted the abundance of H_2O compared to that in von Procházka & Millar (2020).

We would like to thank Jonathan Holdship for his contribution to the chemical modeling, particularly with UCLCHEM's analysis tools. This project has received funding from the European Unions Horizon 2020 research and innovation program under the Marie Skłodowska-Curie grant agreement No 811312 for the project "Astro-Chemical Origins" (ACO). This work is part of a project that has received funding from the European Research Council (ERC) under the European Unions Horizon 2020 research and innovation program MOPPEX 833460.

Appendix

Table A1 details the c_k coefficients used in Equation 1 for the CR ionization rate and the H_2 dissociation rate dependencies. Tables A2–A5 summarize all abundance changes seen and their corresponding conditions.

Table A1
Coefficients from Padovani et al. (2018b) and Padovani et al. (2018a) for the Rate Dependencies

CR Ionization Dependency Coefficients		
k	c_k (model L)	c_k (model H)
0	$1.545456645800 \times 10^7$	$1.223529865309 \times 10^7$
1	$-6.307708626617 \times 10^6$	$-5.013766644305 \times 10^6$
2	$1.142680666041 \times 10^6$	$9.120125566763 \times 10^5$
3	$-1.205932302621 \times 10^5$	$-9.665446168847 \times 10^4$
4	$8.170913352693 \times 10^3$	$6.576930812109 \times 10^3$
5	$-3.686121296079 \times 10^2$	$-2.979875686226 \times 10^2$
6	$1.107203722057 \times 10^1$	$8.989721355058 \times 10^0$
7	$-2.135293914267 \times 10^{-1}$	$-1.741300519598 \times 10^{-1}$
8	$2.399219033781 \times 10^{-3}$	$1.965098116126 \times 10^{-3}$
9	$-1.196664901916 \times 10^{-5}$	$-9.844203439473 \times 10^{-6}$
CR H ₂ Dissociation Dependency Coefficients		
k	c_k (model L)	c_k (model H)
0	$1.582911005330 \times 10^7$	$1.217227462831 \times 10^7$
1	$-6.465722684896 \times 10^6$	$-4.989649250304 \times 10^6$
2	$1.172189025424 \times 10^6$	$9.079152156645 \times 10^5$
3	$-1.237950798073 \times 10^5$	$-9.624890825395 \times 10^4$
4	$8.393404654312 \times 10^3$	$6.551161486120 \times 10^3$
5	$-3.788811358130 \times 10^2$	$-2.968976216187 \times 10^2$
6	$1.138688455029 \times 10^1$	$8.959037875226 \times 10^0$
7	$-2.197136304567 \times 10^{-1}$	$-1.735757324445 \times 10^{-1}$
8	$2.469841278950 \times 10^{-3}$	$1.959267277734 \times 10^{-3}$
9	$-1.232393620924 \times 10^{-5}$	$-9.816996707980 \times 10^{-6}$

Table A2
Results of the Ionization Rate Dependency on Abundances

Density Species	Pre-collapse		Post-collapse							
	10^2 cm^{-3}		10^4 cm^{-3}		10^5 cm^{-3}		10^6 cm^{-3}		10^7 cm^{-3}	
	L	H	L	H	L	H	L	H	L	H
H ₂ O	...	-9.5	...	+5.4	...	+3.6	...	+6.1
CS	-6.2×10^1	-1.1×10^3	...	$+2.4 \times 10^1$...	$+1 \times 10^1$...	$+1.2 \times 10^1$...	+7.1
NH ₃ (_{grain})	...	-7
N ₂ H ⁺	<limit	<limit	+6.8
NH ₃	-6.8	-2.9×10^1	+5.7
CO(_{grain})	<limit	<limit	...	-4.4×10^6	+3.5
HCO ⁺	-4.2	-2.4×10^1	+4.8	...	+8.2
H ₂ O(_{grain})	...	-6.8
CO ₂ (_{grain})	<limit	<limit	...	-5.3×10^3	...	-6.1	-5.7

Note. The values shown represent an increase (+) or a decrease (-) in abundances compared to the basic model and by what factor the abundances differed. This table only shows changes in abundance greater than a factor of 3 and any value marked “< limit” is below the lower abundance limit of 10^{-13} .

Table A3
Results of the Ionization Rate Dependency on Abundances with Varying Parameters

Temperature (K)	Density: Species	Pre-collapse		Post-collapse							
		10^2 cm^{-3}		10^4 cm^{-3}		10^5 cm^{-3}		10^6 cm^{-3}		10^7 cm^{-3}	
		<i>L</i>	<i>H</i>	<i>L</i>	<i>H</i>	<i>L</i>	<i>H</i>	<i>L</i>	<i>H</i>	<i>L</i>	<i>H</i>
20	H ₂ O	+7.2	...	+6.8	...	+5.5
20	CS	-3.8×10^1	-6.7×10^2	...	$+1.8 \times 10^1$...	+8.2	...	+8.7	...	+4.3
20	NH _{3(grain)}	<limit	<limit	...	-5×10^2	...	-3.1
20	N ₂ H ⁺	<limit	<limit	...	-1.3×10^1	...	+5.2	...	$+1.9 \times 10^1$...	+3.8
20	NH ₃	<limit	<limit	...	-4.6×10^1	...	+7.6	...	+3.3
20	CO _(grain)	<limit	<limit	...	-5.5	...	+5.9	...	+6	...	+3.8
20	HCO ⁺	...	-5.9
20	H ₂ O _(grain)	<limit	<limit	+3.6	$+1.3 \times 10^1$
20	CO _{2(grain)}	<limit	<limit	...	-1.8×10^1
30	H ₂ O	+8.4
30	CS	-3.6×10^1	-5.2×10^2	...	+7.8	...	+6	...	+5.3	...	+4
30	NH _{3(grain)}	<limit	<limit	-1.5×10^2
30	N ₂ H ⁺	<limit	<limit	$+1 \times 10^1$
30	NH ₃	<limit	<limit	...	-8.1	+7
30	HCO ⁺	...	-4.4	+3.3
30	H ₂ O _(grain)	<limit	<limit	...	<limit	-3.3
30	CO _{2(grain)}	<limit	<limit	...	<limit	...	-5.4×10^1
Radfield											
10	H ₂ O	...	-3.8	...	+3.9	...	+3.6	...	+6.1
10	CS	-7.7	-1.3×10^1	...	$+3.4 \times 10^1$...	$+1 \times 10^1$...	$+1.2 \times 10^1$...	+7
10	NH _{3(grain)}	<limit	<limit	+3.1
10	N ₂ H ⁺	<limit	<limit	+6.8
10	NH ₃	...	-8.3	+3.4	$+1.6 \times 10^1$	+5.7	...	+3
10	CO _(grain)	<limit	<limit	...	-6.1×10^6	+3.5
10	HCO ⁺	...	-7.6	+4.8	...	+8
10	CO _{2(grain)}	<limit	<limit	...	-2.8×10^3	...	-6.2	-5.8
100	H ₂ O	$+2.8 \times 10^1$...	+3.6	...	+6.1
100	CS	...	-7.4	...	$+1.7 \times 10^1$...	$+1 \times 10^1$...	$+1.2 \times 10^1$...	+6.9
100	N ₂ H ⁺	<limit	<limit	<limit	<limit	...	+6.8
100	NH ₃	+3.8	$+7.2 \times 10^3$	+5.6	...	+3
100	CO _(grain)	<limit	<limit	<limit	<limit	+3.5
100	HCO ⁺	$+3.1 \times 10^1$...	+4.8	...	+8
100	CO _{2(grain)}	<limit	<limit	<limit	<limit	...	-6.2	-5.7
Zeta											
10	H ₂ O	-4.7	-4.1×10^1	...	-7.8	...	+6.4
10	CS	-5.1×10^1	<limit	+4.2	$+1.7 \times 10^1$...	+4.8	...	+3.8
10	NH _{3(grain)}	<limit	<limit	...	-7.4×10^5
10	N ₂ H ⁺	<limit	<limit	...	-9.6	+4.9	...	+3.9
10	NH ₃	-7.1	-1.1×10^2	...	-1.2×10^1
10	CO _(grain)	<limit	<limit	-4.6×10^5	-2.7×10^7	...	-3.8
10	HCO ⁺	-9.7	-6.7×10^1	...	-6.3	+3.8	...	+3.5
10	H ₂ O _(grain)	-5.6	<limit	...	-2.8×10^6
10	CO _{2(grain)}	<limit	<limit	-1.5×10^2	<limit	...	-6.6×10^1
100	H ₂ O	-1.3×10^1	-2.1×10^2	-3.1	-4.6×10^1	...	-4.8	...	+3.6
100	CS	<limit	<limit	...	-1×10^3	+6.2
100	NH _{3(grain)}	<limit	<limit	-4	-1.8×10^1	...	<limit
100	N ₂ H ⁺	<limit	<limit	...	<limit	...	-1.1×10^1
100	NH ₃	-4.4×10^1	-2×10^1	-3.8	-2.1×10^1	...	-8.6
100	CO _(grain)	<limit	<limit	...	<limit	-3.2	-3.9×10^6
100	HCO ⁺	<limit	<limit	...	-3.2×10^1	...	-8.6
100	H ₂ O _(grain)	<limit	<limit	-3.9	-1.4×10^1	...	-4.9×10^5
100	CO _{2(grain)}	<limit	<limit	<limit	<limit	-4.4	<limit	...	-4.6

Note. The values shown represent an increase (+) or a decrease (-) in abundances compared to the basic model and by what factor the abundances differed. This table only shows changes in abundance greater than a factor of 3 and any value marked “< limit” is below the lower abundance limit of 10^{-13} .

Table A4

The Only Conditions Where the Inclusion of the Dissociation Rate Dependency or the Inclusion of Excited Species Had Any Notable Effect on Abundances

Post-collapse									
Dissociation Dependency									
Radfield	Density: Species	10^4 cm^{-3}		10^5 cm^{-3}		10^6 cm^{-3}		10^7 cm^{-3}	
		<i>L</i>	<i>H</i>	<i>L</i>	<i>H</i>	<i>L</i>	<i>H</i>	<i>L</i>	<i>H</i>
100	NH ₃ (_{grain})	+4.6
100	CO(_{grain})	+4.5
100	H ₂ O(_{grain})	+4.5
100	CO ₂ (_{grain})	+4.2
Zeta									
10	CO(_{grain})	+1.4 × 10 ³
Excited Species									
Temperature (K)	Density:	10^4 cm^{-3}		10^5 cm^{-3}		10^6 cm^{-3}		10^7 cm^{-3}	
		<i>L</i>	<i>H</i>	<i>L</i>	<i>H</i>	<i>L</i>	<i>H</i>	<i>L</i>	<i>H</i>
30	N ₂ H ⁺	-3.9
Zeta									
10	CO ₂ (_{grain})	-6.5
100	H ₂ O	+3.7
100	CS	-7 × 10 ¹	...	-1.8 × 10 ³	...	-7.1	...
100	N ₂ H ⁺	+3.5	...	+3.4	...
100	NH ₃	+4.6	...	+3.9	...
100	CO(_{grain})	-1.7 × 10 ⁸	...	-8.1 × 10 ⁹	...	-2.2 × 10 ⁷	...
100	HCO ⁺	-2.3 × 10 ²	...	-4.9 × 10 ³	...	-2.9 × 10 ¹	...
100	H ₂ O(_{grain})	-3.9
100	CO ₂ (_{grain})	-2.2 × 10 ²	...	-1 × 10 ⁴	...	-3.8 × 10 ¹⁰	...





Note. The values shown represent an increase (+) or a decrease (-) in abundances compared to the basic model and by what factor the abundances differed. This table only shows changes in abundance greater than a factor of 3 and any value marked “< limit” is below the lower abundance limit of 10⁻¹⁵.

Table A5
Results of the Combined Dissociation Rate Dependency and Excited Species on Abundances under Standard Conditions and with Varying Parameters

Density: Species	Post-collapse								
	10^4 cm^{-3}		10^5 cm^{-3}		10^6 cm^{-3}		10^7 cm^{-3}		
	<i>L</i>	<i>H</i>	<i>L</i>	<i>H</i>	<i>L</i>	<i>H</i>	<i>L</i>	<i>H</i>	
CO _(grain)	...	-3.3	...	-5.4	...	-6.1	
HCO ⁺	-3.4	...	
H ₂ O _(grain)	...	-4.1	
CO ₂ (grain)	...	-3.6	...	-6.7	-5.9	-3.7	-5	-7.4	
Temperature (K)									
30	N ₂ H ⁺	<limit	+5.8	
Radfield									
10	CO _(grain)	-5.3×10^1	...	-6	...	
10	HCO ⁺	-3.4	...	
10	H ₂ O _(grain)	...	-4	
10	CO ₂ (grain)	...	-3.4	...	-6.7	-5.9	-3.7	-4.8	
100	CO _(grain)	<limit	-5.1×10^1	...	-6	...	
100	HCO ⁺	-3.4	...	
100	CO ₂ (grain)	<limit	<limit	...	-6.8	-5.9	-3.7	-4.9	
Zeta									
10	H ₂ O	+3.5	
10	CS	-2.4×10^2	...	-4.1×10^1	...	
10	NH ₃ (grain)	-3.7	
10	N ₂ H ⁺	+3.2	...	
10	NH ₃	+4.5	...	
10	CO _(grain)	-3.7	<limit	...	-2.4×10^8	...	
10	HCO ⁺	-6.9×10^2	...	-1.2×10^2	...	
10	H ₂ O _(grain)	
10	CO ₂ (grain)	...	<limit	-4.9	-4.9×10^2	...	-2.6×10^2	...	
100	H ₂ O	+3.3	
100	CS	-9×10^4	...	-1.4×10^3	
100	NH ₃ (grain)	-4.8	+4.4	
100	N ₂ H ⁺	...	<limit	+3.6	...	+1.2 × 10 ¹	
100	NH ₃	+4.5	+3	+9.1	
100	CO _(grain)	...	<limit	-9×10^7	...	-3.2×10^1	...	-7.4×10^6	
100	HCO ⁺	-5.9×10^2	...	-2.5×10^5	...	-5.8×10^3	
100	H ₂ O _(grain)	-1.2×10^1	-3.7	...	
100	CO ₂ (grain)	<limit	<limit	-4.9×10^2	...	-4.7×10^5	...	-1.3×10^1	

Note. The values shown represent an increase (+) or a decrease (-) in abundances compared to the basic model and by what factor the abundances differed. This table only shows changes in abundance greater than a factor of 3 and any value marked "< limit" is below the lower abundance limit of 10^{-13} .

ORCID iDs

Ross O'Donoghue  <https://orcid.org/0000-0002-5317-6304>
 Serena Viti  <https://orcid.org/0000-0001-8504-8844>
 Marco Padovani  <https://orcid.org/0000-0003-2303-0096>
 Tomas James  <https://orcid.org/0000-0002-4240-4359>

References

- Abplanalp, M. J., Gozem, S., Krylov, A. I., et al. 2016, *PNAS*, **113**, 28
 Blandford, R., Simeon, P., & Yuan, Y. 2014, *NuPhS*, **256**, 9
 Caselli, P., Vastel, C., Ceccarelli, C., et al. 2008, *A&A*, **492**, 703
 Choi, Y., Lee, J.-E., Bourke, T. L., & II, N. J. E. 2017, *ApJS*, **229**, 38
 Cummings, A. C., Stone, E. C., Heikkilä, B. C., et al. 2016, *ApJ*, **831**, 18
 de Jong, T., & Kamijo, F. 1973, *A&A*, **25**, 363
 Fuente, A., Navarro, D. G., Caselli, P., et al. 2019, *A&A*, **624**, A105
 Gloeckler, G., & Fisk, L. A. 2015, *ApJL*, **806**, L27
 Goldsmith, P. F., & Li, D. 2005, *ApJ*, **622**, 938
 Herbst, E., & Klemperer, W. 1973, *ApJ*, **185**, 505
 Hirahara, Y., Suzuki, H., Yamamoto, S., et al. 1992, *ApJ*, **394**, 539
 Holdship, J., Viti, S., Jiménez-Serra, I., Makrymallis, A., & Priestley, F. 2017, *AJ*, **154**, 38
 Indriolo, N., Geballe, T. R., Oka, T., & McCall, B. J. 2007, *ApJ*, **671**, 1736
 Indriolo, N., & McCall, B. J. 2012, *ApJ*, **745**, 91
 Indriolo, N., & McCall, B. J. 2013, *ChSRv*, **42**, 7763
 Ivlev, A. V., Padovani, M., Galli, D., & Caselli, P. 2015, *ApJ*, **812**, 135
 Ivlev, A. V., Silsbee, K., Padovani, M., & Galli, D. 2021, *ApJ*, **909**, 107
 Kalvāns, J., & Kalnīn, J. R. 2019, *MNRAS*, **486**, 2050
 Kuffmeier, M., Zhao, B., & Caselli, P. 2020, *A&A*, **639**, A86
 Le Petit, F., Ruaud, M., Bron, E., et al. 2016, *A&A*, **585**, A105
 Lee, C. W., Myers, P. C., & Tafalla, M. 1999, *ApJ*, **526**, 788
 Li, D., & Goldsmith, P. F. 2003, *ApJ*, **585**, 823
 McElroy, D., Walsh, C., Markwick, A. J., et al. 2013, *A&A*, **550**, A36
 Montgomery, A. S., Bates, B., & Davies, R. D. 1995, *MNRAS*, **273**, 449
 Neufeld, D. A., Goicoechea, J. R., Sonnentrucker, P., et al. 2010, *A&A*, **521**, L10
 Neufeld, D. A., & Wolfire, M. G. 2017, *ApJ*, **845**, 163
 Öberg, K. I., Boogert, A. C. A., Pontoppidan, K. M., et al. 2011, in Proc. IAU Symp. 280, Ices in Starless and Starforming Cores. (Cambridge: Cambridge Univ. Press), 65
 Oka, T., Geballe, T. R., Goto, M., Usuda, T., & McCall, B. J. 2005, *ApJ*, **632**, 882

- Padovani, M., Galli, D., Hennebelle, P., Commerçon, B., & Joos, M. 2014, *A&A*, **571**, A33
- Padovani, M., Galli, D., Ivlev, A. V., Caselli, P., & Ferrara, A. 2018a, *A&A*, **619**, A144
- Padovani, M., Hennebelle, P., & Galli, D. 2013, *A&A*, **560**, A114
- Padovani, M., Ivlev, A. V., Galli, D., et al. 2020, *SSRv*, **216**, 29
- Padovani, M., Ivlev, A. V., Galli, D., & Caselli, P. 2018b, *A&A*, **614**, A111
- Potgieter, M. 2013, *LRSP*, **10**, 1
- Prasad, S. S., & Tarafdar, S. P. 1983, *ApJ*, **267**, 603
- Rodgers, S. D., & Charnley, S. B. 2001, *ApJ*, **546**, 324
- Shaw, G., Ferland, G. J., Srianand, R., et al. 2008, *ApJ*, **675**, 405
- Silsbee, K., Caselli, P., & Ivlev, A. V. 2021, *MNRAS*, **507**, 6205
- Sipilä, O., Silsbee, K., & Caselli, P. 2021, *ApJ*, **922**, 126
- Sipilä, O., Zhao, B., & Caselli, P. 2020, *A&A*, **640**, A94
- Shingledecker, C. N., & Herbst, E. 2018, *PCCP*, **20**, 5359
- Shingledecker, C. N., Tennis, J., Le Gal, R., & Herbst, E. 2018, *ApJ*, **861**, 20
- Solomon, P. M., & Werner, M. W. 1971, *ApJ*, **165**, 41
- Spitzer, L. J., & Tomasko, M. G. 1968, *ApJ*, **152**, 971
- Stone, E. C., Cummings, A. C., Heikkilä, B. C., & Lal, N. 2019, *NatAs*, **3**, 1013
- van der Werf, P. P., Goss, W. M., & Vanden Bout, P. A. 1988, *A&A*, **201**, 311
- Viti, S., Bayet, E., Hartquist, T. W., et al. 2013, in *Cosmic Rays in Star-Forming Environments* (Vol. 34) ed. D. F. Torres & O. Reimer (Berlin: Springer), 7
- von Procházka, A. A., & Millar, T. J. 2020, *MNRAS*, **501**, 1228